Int. J. Electrochem. Sci., 12 **(2017)** 206 – 217, doi: 10.20964/2017.01.32

International Journal of
ELECTROCHEMICAL
SCIENCE
www.electrochemsci.org

Facile Synthesis of $LiFePO_4$/C with High Tap-density as Cathode for High Performance Lithium Ion Batteries

Lei Yao[1], *Yan Wang*[2], *Jinhua Wu*[1,3], *Mingwu Xiang*[1], *Jianlong Li*[1], *Boya Wang*[1], *Yun Zhang*[1], *Hao Wu*[1], *Heng Liu*[1,*]

[1] College of Materials Science and Engineering, Sichuan University, Chengdu 610064, PR China
[2] College of Computer Science and Technology, Southwest University for Nationalities, Chengdu 610041, PR China
[3] Department of Materials Engineering, Sichuan College of Architectural Technology, Deyang 618000, PR China
[*]E-mail: h_liu@scu.edu.cn

Received: 1 October 2016 / *Accepted:* 16 November 2016 / *Published:* 12 December 2016

$LiFePO_4$/C cathode materials with a high tap-density originated from $FePO_4 \cdot 2H_2O$ precursors were prepared via a high-temperature solid-phase carbothermic reduction using low-cost Ferroferric oxide (Fe_3O_4) and phosphoric acid (H_3PO_4) as reaction materials. The as-obtained precursors are consistent with $FePO_4 \cdot 2H_2O$ phase with a Pcab space group and no impurity peaks are detected by XRD. The $FePO_4 \cdot 2H_2O$ precursor prepared at 90°C for 8 h and the corresponding $LiFePO_4$/C composite show high tap-density of 1.45 g cm^{-3} and 1.36 g cm^{-3}, respectively. The $LiFePO_4$/C delivers a high initial discharge capacity of 159 mAh g^{-1} at 0.1 C. Meanwhile, an initial capacity of 95 mAh g^{-1} and superior capacity retention of 96.3 % are retained after 70 cycles at a high rate of 10 C.

Keywords: $LiFePO_4$/C, $FePO_4 \cdot 2H_2O$ precursors, Fe_3O_4, lithium ion batteries

1. INTRODUCTION

Olivine-structured lithium iron phosphate ($LiFePO_4$) is viewed as the most promising cathode materials for lithium ion batteries (LIBs) due to its relatively high theoretical capacity of 170 mAh g^{-1}, excellent thermal stability, low cost, high security and environmental friendliness [1-3]. Hence, $LiFePO_4$ as significant cathode materials has been widely applied to electric vehicle (EVs) [4], hybrid electric vehicles (HEVs) [5] and energy storage system [6]. However, $LiFePO_4$ without modification shows a very low electric conductivity (about 10^{-9} S cm^{-1}), directly leading to a poor rate performance [7, 8]. Therefore, many researchers have devoted considerable efforts to help improve the electronic

conductivity of $LiFePO_4$, such as conductive polymer or carbon coating [9, 10], nanosized particles optimization [11, 12] and supervalent cations doping [13, 14]. Among these strategies, conductive carbon layer coating is usually employed as the most effective approach to improve the electrical conductivity of $LiFePO_4$ [15, 16]. In addition, the low tap-density of $LiFePO_4$/C leads to a significantly decrease of volumetric energy density, hindering its extensive application in high energy storage fields. The morphology and size distribution of $LiFePO_4$ particles play an important role in the improvement of tap-density. Generally, spherical particles with a homogeneous size distribution have higher tap-density than the irregular [17-19]. In view of this viewpoint, some special methods such as solvothermal [20], sol spray-drying [19] and rheological phase [21] have been used as effective synthesizing routes to synthesize the spherical $LiFePO_4$ cathode materials. However, these synthesis methods could be hindered for extensive applications due to high cost reaction reagent and equipment, complex synthetic steps and low yield.

In this work, $LiFePO_4$/C cathode materials with high tap-density were prepared by a facile high-temperature solid-phase carbothermic reduction using low-cost Fe_3O_4 and H_3PO_4 as raw materials. A stearic acid was used as a carbon source and reductive agent to carry out the carbon coating layer. Effects of reaction time on morphology, structure and mole ratio of Fe/P of $FePO_4{\cdot}2H_2O$ precursors were investigated in detail. The resulting $LiFePO_4$/C shows an improved rate capacity and cycling performance.

2. EXPERIMENTAL

2.1 Preparation of materials

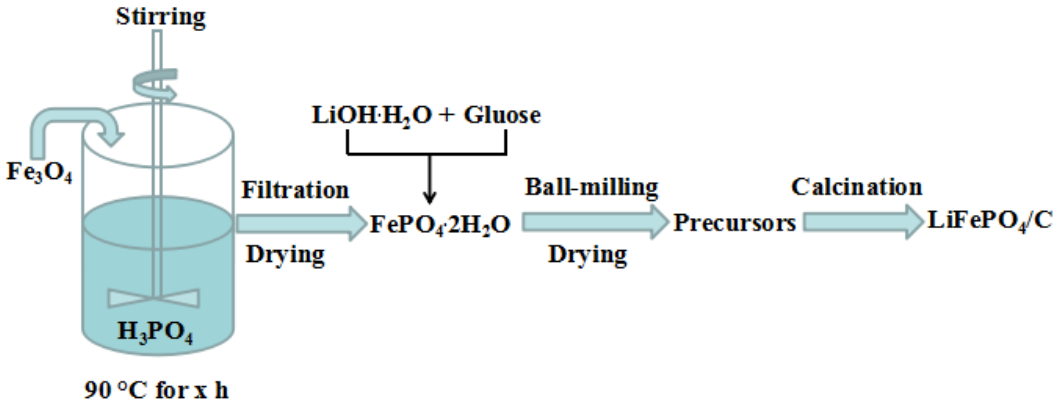

Figure 1. Schematic representation of the synthesis processes of $FePO_4{\cdot}2H_2O$ precursor and $LiFePO_4$/C.

Fig. 1 depicts the synthesis processes of the $FePO_4{\cdot}2H_2O$ precursors and $LiFePO_4$/C. $FePO_4{\cdot}2H_2O$ precursors were firstly prepared by continuously stirring the Fe_3O_4 and H_3PO_4 in aqueous solution at 90°C for different time. The Fe/P molar ratio of 1:3 is always controlled to guarantee a complete reaction during the whole reaction process. After filtrating, washing and drying at 85°C for 8 h, a white $FePO_4{\cdot}2H_2O$ precursor was obtained.

The $LiFePO_4$/C composites were synthesized via a high-temperature solid-phase carbothermic reduction method. $FePO_4 \cdot 2H_2O$ precursor, Stearic acid and $LiOH \cdot H_2O$ were mixed in alcohol solution by ball-milling for 3 h to form a homogeneous orange-yellow slurry mixture. After drying at 70°C for 8 h the mixture was calcined at 350°C for 2 h and then 700°C for 10 h under N_2 atmosphere. Finally, the $LiFePO_4$/C composites were obtained after cooling down to room temperature. To simplify the as-prepared samples, $FePO_4 \cdot 2H_2O$ precursors prepared at different reaction time of 4 h, 6 h, 8 h and 10 h were marked as FP-4, FP-6, FP-8 and FP-10, respectively. And the corresponding $LiFePO_4$/C composites were signed as LFP-4, LFP-6, LFP-8 and LFP-10, respectively.

2.2 Characterization

Crystalline phase of all synthesized materials was identified by X-ray diffraction (XRD, Phlips X' pert TROMPD, Cu Kα radiation, $\lambda = 1.54178$ Å). Morphology was examined by a field-emission transmission electron microscope (Libra200FE) and a field-emission scanning electron microscopy (FE-SEM, HitachiS-4800). The tap-density of $FePO_4 \cdot 2H_2O$ precursors and $LiFePO_4$/C materials were tested by powder tap-density meter (JZ-1, RooKo Instrument, China). Median diameter of the powers was determined using a laser particle analyzer (JL-1177). The composition was analyzed using an inductively coupled plasma source mass spectrometer (ICPMS7700, Agilent, USA). Carbon content in the $LiFePO_4$/C composites was defined by chemical analysis and carbon property was investigated by Raman spectroscopy (LabRAM HR).

2.3 Electrochemical measurements

The electrochemical tests were investigated by assembling CR2032 coin-type cells. For the fabrication of cathode electrodes, $LiFePO_4$/C, acetylene black and PVDF binder in a weight ratio of 80:10:10 were mixed to form homogeneous slurries and then coated on Al foil current collector. After drying at 120°C for 12 h in a vacuum, the final film was punched into disc with the diameter of 14 mm as the cathode. Lithium foil served as the counter electrode and Celgard 2400 membrane was used as the separator. The electrolyte is consisted of a solution of 1 M $LiPF_6$ in ethylene carbonate (EC)/diethyl carbonate (DEC) (1:1 by volume). Coin cells were assembled in an argon-filled glove box. The charge/discharge performance was carried out by an automatic NEWARE battery cycler (Neware BTS-610) in a voltage range of 2.5-4.3 V at room temperature. Cyclic voltammetry (CV) were conducted using a Gamry PCI 4750 electrochemical workstation in the voltage range of 2.5-4.3 V with a scan rate of 0.1mV s^{-1}. Electrochemical impedance spectroscopy (EIS) was carried out on an electrochemical workstation (CHI660D, China) at frequencies from 100 kHz to 0.01 Hz with a perturbation amplitude of 5 mV.

3. RESULTS AND DISCUSSION

Fig. 2(a) and (b) show the crystal structure and particle morphology of Fe_3O_4, respectively. As shown in Fig. 2(a), all characteristic diffraction peaks of Fe_3O_4 can be well indexed to be an ordered

spinel structure with an Fd3m space group (PDF file No. 88-0315). No other impurities are detected. Fig. 2(b) exhibits a typical cubic morphology with a size distribution of 500 nm to 1 μm. Fig. 3 depicts the XRD spectra of $FePO_4 \cdot 2H_2O$ precursors prepared at different reaction time, all the precursors are indexed to be a well crystallized $FePO_4 \cdot 2H_2O$ phase with a Pcab space group (PDF file No. 33-0667) and no obvious impurity peaks are observed, indicating that $FePO_4 \cdot 2H_2O$ precursors with good crystallinity are synthesized successfully.

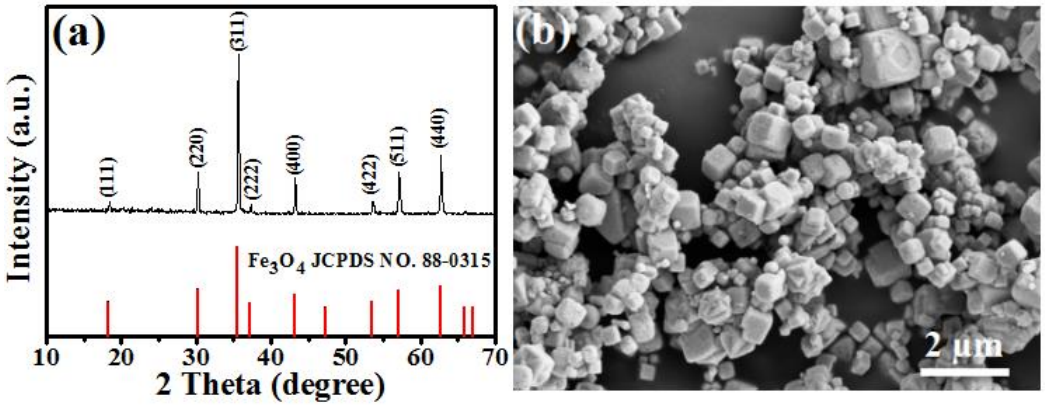

Figure 2.(a) XRD pattern and (b) SEM image of Fe_3O_4.

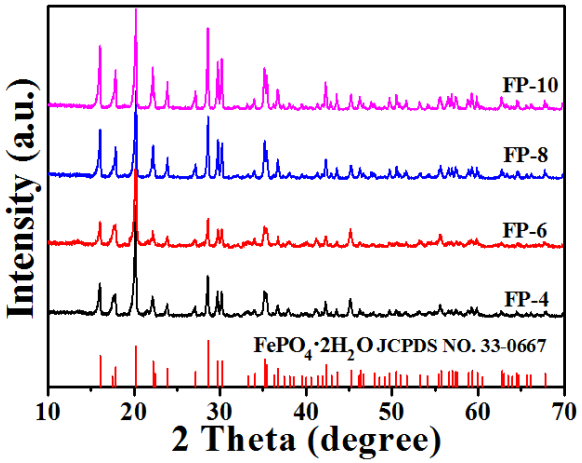

Figure 3. XRD patterns of FP-4, FP-6, FP-8 and FP-10.

The median diameter (D_{50}), tap-density and mole ratios of Fe/P of $FePO_4 \cdot 2H_2O$ precursors prepared at different reaction time are showed in table 1.

Table 1. Median diameter (D_{50}), Tap-density and Mole ratios of Fe/P of $FePO_4 \cdot 2H_2O$ precursors.

Samples	FP-4	FP-6	FP-8	FP-10
D_{50} (μm)	33.0	29.6	28.0	23.3
Tap density (g cm^{-3})	1.58	1.40	1.45	1.41
Mole ratio of Fe/P	1.0226	1.0093	0.9989	0.9963

All $FePO_4{\cdot}2H_2O$ precursors show a high tap-density over 1.4 cm^3 g^{-1}. In particular, the $FePO_4{\cdot}2H_2O$ precursor prepared at 4 h shows a much higher tap-density of 1.58 g cm^{-3}. After increasing the reaction time from 6 to 10 h, the tap-density has no obvious change. However, the D_{50} reveals a significantly decrease with the extension of reaction time, indicating that much smaller $FePO_4{\cdot}2H_2O$ particles are generated. The mole ratios of Fe/P of $FePO_4{\cdot}2H_2O$ precursors are also measured. It can be found that both FP-4 and LP-6 deliver a higher specific value of Fe/P than 1 which means short reaction time resulting in incomplete reaction process. Extending reaction time to 8 and 10 h, the mole ratio of Fe/P start to falling and show appropriate values range from 0.99 to 1. Meanwhile, FP-8 delivers a higher value than FP-10. It has been reported that high purity $FePO_4{\cdot}2H_2O$ precursor display favorable impact on the performance of corresponding $LiFePO_4$/C material [22].

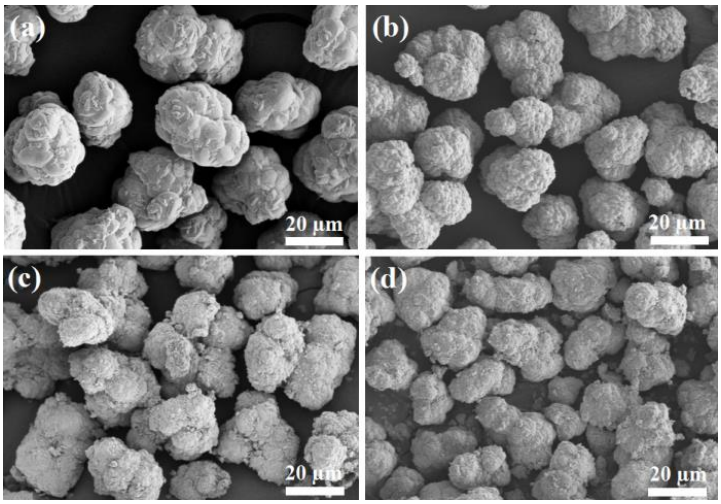

Figure 4. SEM images of (a) FP-4, (b) FP-6, (c) FP-8 and (d) FP-10.

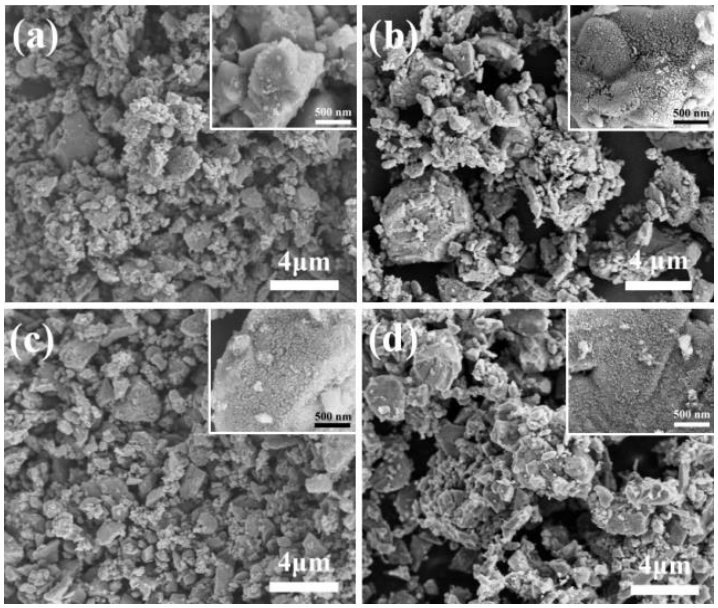

Figure 5. SEM images of (a) LFP-4, (b) LFP-6, (c) LFP-8 and (d) LFP-10.

Fig. 4 shows SEM images of FP-4, FP-6, FP-8 and FP-10, respectively. All the $FePO_4 \cdot 2H_2O$ precursors have a homogeneous particles size distribution and an analogous spherical morphology, which is formed from the agglomeration of smaller primary particle. Obviously, the particles size decreased with the increasing of reaction time, which is well corresponding to the D_{50} in table 1. For FP-8 and FP-10 samples, there exist some broken small particles on the surface of large agglomeration particles. However, the FP-4 prepared at relatively short reaction time exhibits an intact analogous spherical structure with a large average particles size of 33 μm, showing a higher tap-density.

Fig. 5 depicts the morphology and microstructure of LFP-4, LFP-6, LFP-8 and LFP-10, respectively. Through the same ball milling time and calcination process, the analogous morphology originated from $FePO_4 \cdot 2H_2O$ precursors is not well inherited, while all the $LiFePO_4$/C materials show irregular particle morphology with similar large and small particles. Interestingly, the small particles can fill in the gaps between large particles formed by the severe agglomeration of much smaller particles, leading to the tap-density improvement of $LiFePO_4$/C materials. The tap-densities of LFP-4, LFP-6, LFP-8 and LFP-10 are 1.38, 1.34, 1.36 and 1.35 g cm^{-3}, respectively.

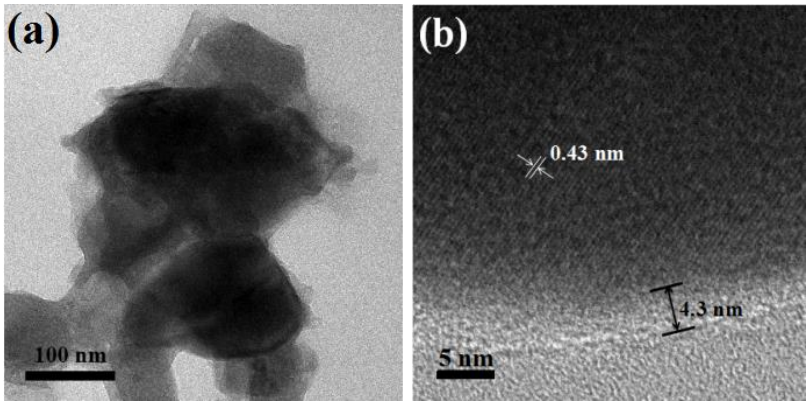

Figure 6.(a) TEM and (b) HRTEM images of sample LFP-8.

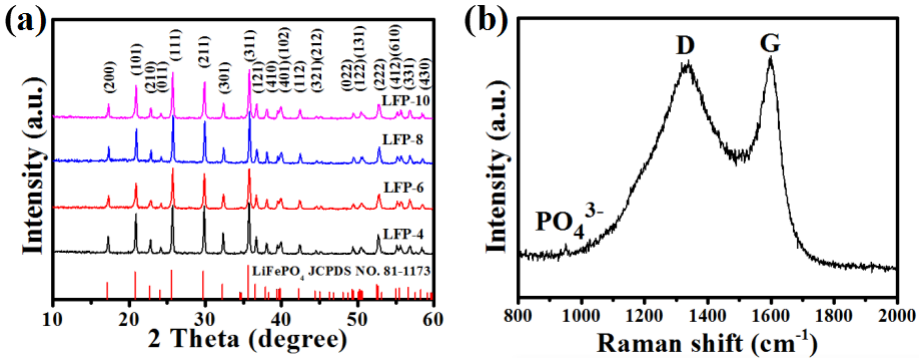

Figure 7.(a) XRD patterns of LFP-4, LFP-6, LFP-8 and LFP-10. (b) Raman spectra of LFP-8.

TEM and HRTEM are carried out to further define the particles microstructure and the amorphous carbon layer coating of the LFP-8 sample, as shown in Fig. 6(a) and (b). The $LiFePO_4$

particles are surrounded by a continuous carbon network, which restraining the particles growth. Therefore, the small particles with a size of about 100 nm are helpful to shorten the ionic and electrical pathway for LIBs [23]. As shown in Fig. 6(b), the $LiFePO_4$ particle shows a uniform and thin carbon coating layer (about 4.3 nm). Regular lattice fringes arrangement can be observed clearly and the fringes distance is about 0.43 nm, which is in accordance with the (101) crystalline plan of $LiFePO_4$ (PDF file No. 81-1173).

Fig. 7(a) shows the XRD patterns of $LiFePO_4$/C composite materials derived from different $FePO_4 \cdot 2H_2O$ precursors. The diffraction peaks of all $LiFePO_4$/C materials can be identified to be an orthorhombic olivine structure with a space group of Pnma (PDF file No. 81-1173). All as-obtained $LiFePO_4$/C composites present high diffraction peaks intensity and narrow full-width at half-maximum (FWHM), indicating high crystallinity of $LiFePO_4$/C materials. No obvious impurity phases are detected, indicating that the crystalline structure of $LiFePO_4$ is not significantly changed after coating a carbon layer. Lattice parameters are calculated based on the XRD data and summarized in Table 2.

Table 2. Lattice parameters and cell volume of LFP-4, LFP-6, LFP-8 and LFP-10.

Samples	a(Å)	b(Å)	c(Å)	V(Å^3)
LFP-4	5.985	10.301	4.683	288.73
LFP-6	5.980	10.230	4.683	287.87
LFP-8	5.976	10.291	4.669	287.13
LFP-10	5.983	10.297	4.678	288.09

The LFP-8 sample shows a smaller lattice parameters and cell volume, suggesting a slight lattice contraction due to the crystal defects caused by the existence of lithium vacancies. Carbon layer coating plays an important role in the electrochemical performance of $LiFePO_4$/C materials [24, 25]. Therefore, Raman spectrum is used to characterize the residual carbon property, as shown in Fig. 7(b). Two bands located at 1350 and 1593 cm^{-1} are attributed to the disorder/defect (D-band) and graphitic carbon (G-band) [26], suggesting that stearic acid is notably carbonized after the high temperature calcination [27]. An additional weak peak located at about 950 cm^{-1} was also detected, which is designated to the symmetric PO_4 stretching mode in $LiFePO_4$ [28]. The coating carbon with lower I_D/I_G ratios demonstrates a higher graphitization degree, indicating a better electrical conductivity [3, 29]. In particular, the LFP-8 sample shows a high degree of graphitization due to the high I_G (I_D/I_G = 0.96). Elemental analysis reveals that the amounts of carbon are 3.41 w%, 3.39 w%, 3.44 w% and 3.42 w% for LFP-4, LFP-6, LFP-8 and LFP-10, respectively.

Fig. 8 exhibits the galvanostatic initial charge-discharge curves of $LiFePO_4$/C materials at various rates from 0.1 to 10 C in the voltage range of 2.5-4.3 V. All samples exhibit the typical charge/discharge plateau of $LiFePO_4$/C cathode materials at about 3.40 V and 3.44 V. At a low rate of 0.1 C, the initial capacities are 139, 144, 159 and 163mAh g^{-1} for LFP-4, LFP-6, LFP-8 and LFP-10, respectively. At a high rate of 10 C, LFP-4, LFP-6 and LFP-10 deliver discharge specific capacities of 59, 66 and 81 mAh g^{-1}, while LFP-8 sample can retain a high capacity of 93 mAh g^{-1}, indicating an

improved rate performance. Such excellent rate capacity for LFP-8 sample is attributed to corresponding high purity $FePO_4 \cdot 2H_2O$ precursor and high carbon content.

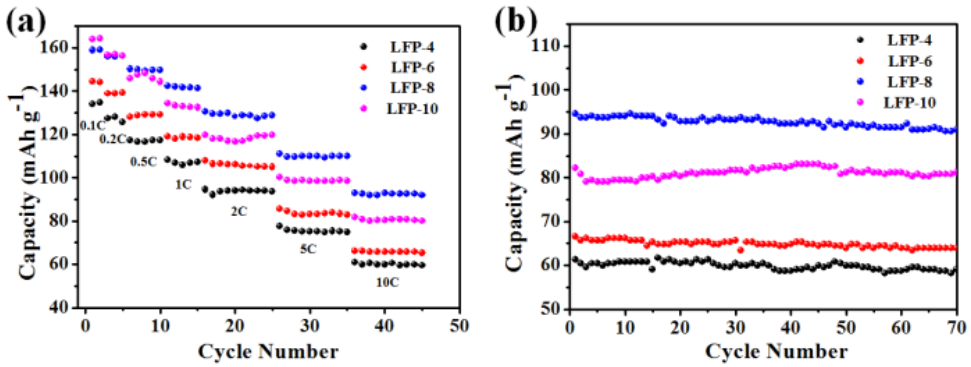

Figure 8. The initial charge/discharge profiles of (a) LFP-4, (b) LFP-6, (c) LFP-8 and (d) LFP-10 at different rates between 0.1 C and 10 C.

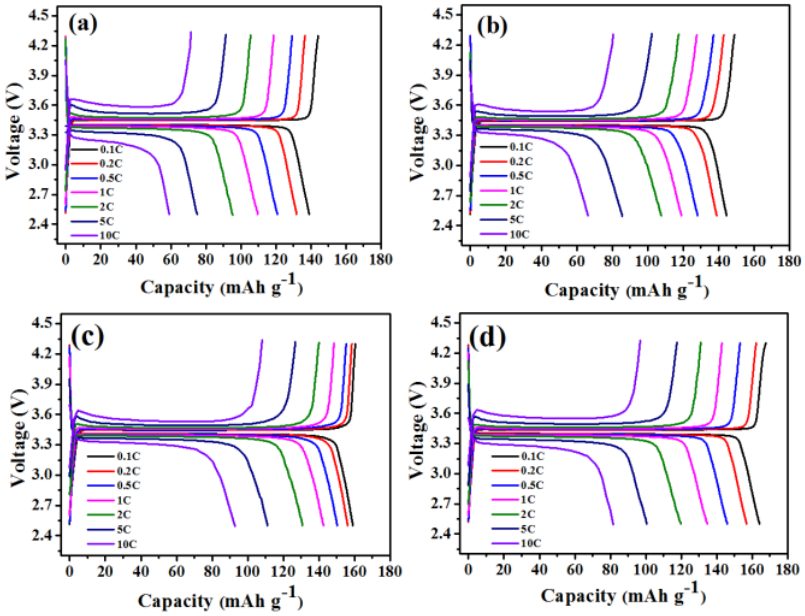

Figure 9.(a) The rate capacities of $LiFePO_4$/C cathodes at various rates and (b) the cycling performances of $LiFePO_4$/C cathodes at 10 C.

Fig. 9(a) shows the rate capacities of LFP-4, LFP-6, LFP-8 and LFP-10 cathodes from 0.1 C to 10 C, respectively. With the increasing of C rate, the rate capacities for all as-prepared $LiFePO_4$/C cathodes decreased. The LFP-8 shows a good rate performance with reversible capacities of 150, 142, 130, 111 and 93 mAh g^{-1} at 0.5 C, 1 C, 2 C, 5 C and 10 C, respectively. Fig. 9(b) shows the cycling performance of $LiFePO_4$/C cathodes at 10 C. The LFP-4, LFP-6, LFP-8 and LFP-10 cathodes deliver the first discharge specific capacities of 61, 67, 95 and 81 mAh g^{-1} and obtain the high capacity retention of 95.7, 95.9, 96.3 and 95.3 % after 70 cycles, respectively. The excellent cycling performance of LFP-8 sample could be ascribed to its unique structure such as homogeneous particles

distribution and thin carbon coating layer, which effectively improving the electrical conductivity and restraining the $LiFePO_4$ dissolution into the organic electrolyte.

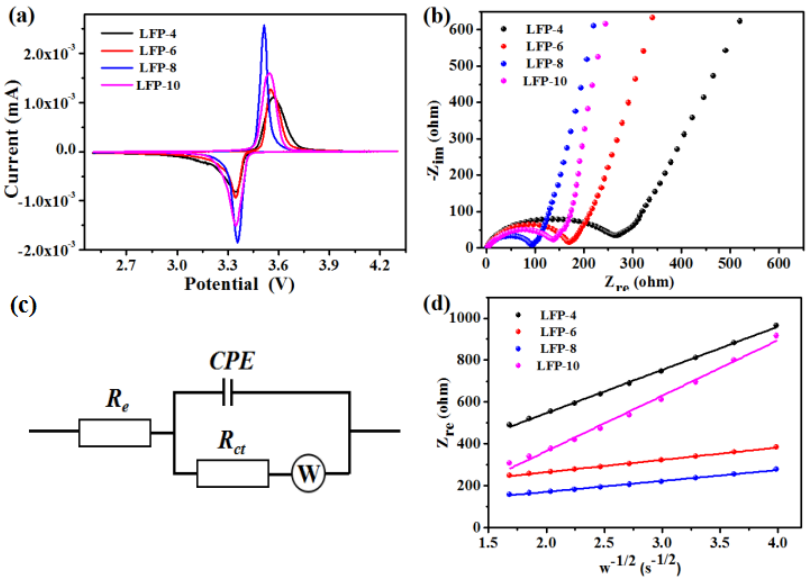

Figure 10.(a) The CV curves of $LiFePO_4$/C cathodes at a scan rate of 0.1 mV s^{-1}, (b) the impedance spectra of $LiFePO_4$/C cathodes, (c) the equivalent circuit derived from impedance spectra (d) the relationship between resistance (Z) and frequency square root ($\omega^{-1/2}$).

Fig. 10(a) shows the CV profiles of $LiFePO_4$/C composites in the voltage range from 2.5-4.3 V at a scan rate of 0.1 mV s^{-1}. All the $LiFePO_4$/C cathodes have the similar CV curves with one pair of redox peaks located at about 3.35 V and 3.53 V, respectively. The one pair of redox peaks are well consistent with the charge/discharge plateaus (Fig. 8), further confirming the important lithium ion intercalation/deintercalation process of $LiFePO_4$/C in LIBs [30]. Moreover, the LFP-8 sample shows a high peak current and a low potential difference (0.16 V), which is less than 0.22 V, 0.20 V and 0.19 V for LFP-4, LFP-6 and LFP-10, respectively. This result implies that the LFP-8 sample exhibits a good reversibility with an extremely low polarization corresponding to the best rate and cycling performance. To further investigate the kinetic processes of the $LiFePO_4$/C cathodes, electrochemical impedance spectroscopy (EIS) is carried out in the frequency range from 0.01 Hz to 100 kHz. As shown in Fig. 10(b), the Nyquist plots are composed of a semicircle at high-to-middle frequency range and an inclined line within the low frequency range. The semicircle represents interface charge transfer resistance (R_{ct}), and the inclined line corresponds to Warburg impedance (W_o). In addition, the intercept at real axis in high-frequency reflects the ohmic resistance (R_e), including the electrolyte and intrinsic electrode resistances [31, 32]. The Nyquist plots are fitted using the equivalent circuit showed in Fig. 10(c) and the fitting results are represented in Table 3.

Table 3. The resistance and lithium-ion coefficient of LFP-4, LFP-6, LFP-8 and LFP-10.

Samples	$R_e(\Omega)$	$R_{ct}(\Omega)$	$D(cm^2\ s^{-1})$
LFP-4	2.52	261	7.37×10^{-15}
LFP-6	2.01	168	8.26×10^{-14}
LFP-8	2.59	90	1.14×10^{-13}
LFP-10	3.23	134	5.52×10^{-15}

All samples reveal a low and similar ohmic resistance. However, from LFP-4 to LFP-10, the R_{ct} is firstly reduced and then increased. The LFP-8 shows a smaller charge transfer resistance of 90 Ω, indicating fast Li^+ ions transmission in the LFP-8 cathode. The so-called Warburg impedance is attributed to the diffusion of the Li^+ ions into the bulk of the electrode material and the Warburg coefficient σ can be obtained by the following equation [33] (1):

$$Z_{re} = R_e + R_{ct} + \sigma\omega^{-1/2} \quad (1)$$

Where R_e is the resistance of the electrolyte, R_{ct} is the charge transfer resistance and the ω is the angular frequency in the low frequency region. Both R_e and R_{ct} are kinetics parameters. σ is the slope for the plot of Z_{re} vs. the reciprocal root square of the lower angular frequencies ($\omega^{-1/2}$), as shown in Fig. 10(d). The slope corresponds to the Warburg coefficient σ. In addition, the Li-ion diffusion rate (D) is determined by the following equation [34-36] (2):

$$D=R^2T^2/2A^2n^4F^4C^2\sigma^2 \quad (2)$$

Where R is the gas constant, *T* is absolute temperature (K), F is the Faraday constant, A is the surface area of $LiFePO_4$ cathode, n is the number of electrons during the process of Li-ion transportation, C is the molar concentration of Li-ion in the $LiFePO_4$ cathode and σ is the Warburg coefficient. The Li-ion diffusion coefficients of LFP-4, LFP-6, LFP-8 and LFP-10 are calculated to be 7.37×10^{-15}, 8.26×10^{-14}, 1.14×10^{-13} and 5.52×10^{-15} $cm^2\ s^{-1}$, respectively, as shown in Table 3. The LFP-8 sample shows a higher Li-ion diffusion coefficient, further confirming the low charge transfer resistance, suggesting a facile insertion/extraction of Li^+ ions in LFP-8 cathode. This result may be a reasonable cause to explain the excellent rate capacity and cycling performance for the LFP-8 cathode.

4. CONCLUSION

In this work, high tap-density $LiFePO_4$/C cathode materials were synthesized by a facile high-temperature solid-phase carbothermic reduction using low-cost ferroferric oxide (Fe_3O_4) as iron source. Reaction time of the $FePO_4{\cdot}2H_2O$ precursors has a significant influence on the morphology, structure and mole ratio of Fe/P. The as-obtained $FePO_4{\cdot}2H_2O$ precursors have analogous spherical morphology with a homogeneous particles size distribution. The resulting LFP-8 has a high tap-density of 1.36 g cm^{-3} and appropriate carbon coating layer, exhibiting superior cycling and rate performance. The LFP-8 can deliver a high initial discharge specific capacity of 159 mAh g^{-1} at 0.1 C. Even at a high rate of 10 C, a reversible capacity of 93 mAh g^{-1} and retention rate of 96.3 % are obtained after 70 cycles.

ACKNOWLEDGEMENT
This work was supported by the the Sichuan Province Science & Technology Foundation of China (2014GZ0094).

References

1. A.K. Padhi, K.S. Nanjundaswamy, J.B. Goodenough, *J. Electrochem. Soc.*, 144 (1997) 1188-1194.
2. H. Nakano, K. Dokko, S. Koizumi, H. Tannai, K. Kanamura, *J. Electrochem. Soc.*, 155 (2008) A909-A914.
3. M.M. Doeff, Y.Q. Hu, F. McLarnon, R. Kostecki, *Electrochem. Solid-State Lett.*, 6 (2003) A207-A209.
4. A. Marongiu, D.U. Sauer, *Int. J. Automot. Technol.*, 17 (2016) 465-472.
5. F.T. Siang, W.T. Chee, *Renew. Sustain. Energy Rev.*, 20 (2013) 82-102.
6. Z.Y. Song, H. Hofmann, J.Q. Li, J. Hou, X.W. Zhang, M. Ouyang, *Appl. Energy*, 159 (2015) 576-588.
7. J.C. Lu, G. Oyama, S.-I. Nishimura, A. Yamada, *Chem. Mater.*, 28 (2016) 1101-1106.
8. K.-M. Kang, H.W. Kim, H.-Y. Kwak, *Korean J. Chem. Eng.*, 32 (2016) 688-696.
9. C.L. Gong, Z.G. Xue, S. Wen, Y.S. Ye, X.L. Xie, *J. Power Sources*, 318 (2016) 93-112.
10. W. Li, J. Hwang, W. Chang, H. Setiadi, K.Y. Chung, J. Kim, *J. of Supercritical Fluids*, 116 (2016) 164-171.
11. K. Bazzi, M. Nazri, V.M. NaiK, V.K. Garg, A.C. Oliveira, P.P. Vaishnava, G.A. Nazri, R. Naik, *J. Power Sources*, 306 (2016) 17-23.
12. K. Naoi, K. Kisu, E. Iwama, S. Nakashima, Y. Sakai, Y. Orikasa, P. Leone, N. Dupre, T. Brousse, P. Rozier, *Energy Environ. Sci.*, 9 (2016) 2143-2151.
13. C.H. Zhang, Y.Z. Liang, L. Yao, Y.P. Qiu, *Solid State Ionics*, 267 (2014) 74-79.
14. Y. Gan, C. Chen, J.L. Liu, P.W. Bian, H. Hao, A.S. Yu, *J. Alloy. Compd.*, 620 (2015) 350-357.
15. F. Wen, H.B. Shu, Y.Y. Zhang, J.J. Wan, W.H. Huang, X.K. Yang, R.Z. Yu, L. Liu, X.Y. Wang, *Electrochim. Acta*, 214 (2016) 85-93.
16. J. Chen, N. Zhao, G.-D. Li, F.-F. Guo, X.F. Wang, T.K. Jia, J.W. Zhao, Y.G. Zhao, X.L. Wang, L. Wan, *Mater. Chem. Phys.*, 180 (2016) 244-249.
17. Y. Jin, X.C. Tang, H.Y. Wang, *Rsc Adv*, 6 (2016) 75602-75608.
18. N.B. Bai, H. Chen, W. Zhou, K.X. Xiang, Y.L. Zhang, C.L. Li, H.Y. Lu, *Electrochim. Acta*, 167 (2015) 172-178.
19. L. Wu, S.K. Zhong, J.Q. Liu, F. Lv, K. Wan, *Mater. Lett.*, 89 (2012) 32-35.
20. W. Wei, D.Z. Chen, R.N. Wang, L. Guo, *Nanotech*, 23 (2012) 475401.
21. X.M. Lou, Y.X. Zhang, *J. Mater. Chem.*, 21 (2011) 4156-4160.
22. N.N. Zhao, Y.S. Li, X.X. Zhao, X.K. Zhi, G.C. Liang, *J. Alloy. Compd.*, 683 (2016) 123-132.
23. M.F. Chen, X.Y. Wang, H.B. Shu, R.Z. Yu, X.K. Yang, W.H. Huang, *J. Alloy. Compd.*, 652 (2015) 213-219.
24. Y.-F. Wu, Y.-N. Liu, S.-W. Guo, S.-N. Zhang, T.-N. Lu, Z.-M. Yu, C.-S. Li, Z.-P. Xi, *J. Power Sources*, 256 (2014) 336-344.
25. G.H. Qin, Q.Q. Ma, C.Y. Wang, *Solid State Ionics*, 257 (2014) 60-66.
26. C.M. Burba, J.M. Palmer, B.S. Holinsworth, *J. Raman Spectrosc.*, 40 (2009) 225-228.
27. G. Wu, R. Ran, B.T. Zhao, Y.J. Sha, C. Su, Y.K. Zhou, Z.P. Shao, *J. Energ. Chem.*, 23 (2014) 363-
28. G.T.K. Fey, T.L. Lu, F.Y. Wu, W.H. Li, *J. Solid State Electrochem.*, 12 (2008) 825-833.
29. M.M. Doeff, J.D. Wilcox, R. Kostecki, G. Lau, *J. Power Sources*, 163 (2006) 180-184.
30. Q. Zhang, S.-Z. Huang, J. Jin, J. Liu, Y. Li, H.-E. Wang, L.-H. Chen, B.-J. Wang, B.-L. Su, *Sci. Rep.*, 6 (2016) 25942.
31. H. Gong, H.R. Xue, T. Wang, J.P. He, *J. Power Sources*, 318 (2016) 220-227.

32. Z.Y. Chen, Q.F. Zhao, M. Xu, L.J. Li, J.F. Duan, H.L. Zhou, *Electrochim. Acta*, 186 (2015) 117-124.
33. Y. Cui, X.L. Zhao, R.S. Guo, *Electrochim. Acta*, 55 (2010) 922-926.
34. K. Tang, X.Q. Yu, J.P. Sun, H. Li, X.J. Huang, *Electrochim. Acta*, 56 (2011) 4869-4875.
35. A.Y. Shenouda, H.K. Liu, *J. Power Sources*, 185 (2008) 1386-1391.
36. A.Y. Shenouda, H.K. Liu, *J. Alloys Compd.*, 477 (2009) 498-503.